

Hydrogen Two-Photon Continuum Emission from the Horseshoe Filament in NGC 1275

R.M. Johnstone^{1*}, R.E.A. Canning¹, A.C. Fabian¹, G.J. Ferland², M. Lykins²,
R.L. Porter³, P.A.M. van Hoof⁴ and R.J.R Williams⁵

¹Institute of Astronomy, University of Cambridge, Madingley Road, Cambridge CB3 0HA

²Department of Physics, University of Kentucky, Lexington, KY 40506, USA

³Department of Physics and Astronomy and Center for Simulational Physics, The University of Georgia, Athens, GA 30602-2451, USA

⁴Royal Observatory of Belgium, Ringlaan 3, 1180 Brussels, Belgium

⁵AWE plc, Aldermaston, Reading RG7 4PR

Received

ABSTRACT

Far ultraviolet emission has been detected from a knot of H α emission in the Horseshoe filament, far out in the NGC 1275 nebula. The flux detected relative to the brightness of the H α line in the same spatial region is very close to that expected from Hydrogen two-photon continuum emission in the particle heating model of Ferland et al. (2009) if reddening internal to the filaments is taken into account. We find no need to invoke other sources of far ultraviolet emission such as hot stars or emission lines from CIV in intermediate temperature gas to explain these data.

Key words: galaxies: clusters: individual: Perseus – galaxies: individual: NGC 1275 – intergalactic medium – ultraviolet: ISM

1 INTRODUCTION

Many central galaxies in cool core clusters exhibit an extensive optical emission-line nebula. The best observed example of such a system is in NGC 1275 which lies at the centre of the Perseus Cluster. The optical emission-line spectrum shows a characteristic low-ionization state similar to that seen in Low Ionization Nuclear Emission-Line Regions (LINERs); many authors have sought to understand the excitation and ionization mechanism of this gas. The line spectrum is rich and there are many potential diagnostics present.

Recently, the field has become confused because, in the nearby systems that we can observe in detail (eg NGC 4696 in the Centaurus Cluster and NGC 1275 in the Perseus Cluster), it is clear that different processes are at work in different spatial regions. Depending on the redshift of the source, the instrument and the exposure times being used different parts of the nebula will be detected. For example, in early works such as Johnstone, Fabian, & Nulsen (1987) which used smaller telescopes and relatively short exposure times the emission lines were detected mainly from the very central part of the galaxy. There, it was found that an excess of blue light over that expected from a normal elliptical galaxy correlated quantitatively with the luminosity in H α , strongly suggesting the presence of star formation. Star formation is also clearly at work in some regions which are much further out (e.g. Canning et al. 2010).

Most central cluster galaxies are host to a radio source, indi-

cating the presence of an active nucleus. Although in most cases the accretion luminosity from the black hole is many orders of magnitude lower than expected from accretion at the Bondi rate (Di Matteo et al. 2001) there are some sources which are clearly dominated by lines from the active nucleus in their central regions (eg broad lines in Abell 1068, Hatch, Crawford, & Fabian 2007; strong [OIII] λ 5007 emission in NGC 1275, Johnstone & Fabian 1988; strong [OIII] λ 5007 emission, Abell 3581 Farage, McGregor, & Dopita 2012).

In a series of papers starting with Johnstone et al. (2007) we are focussing on the emission line spectrum from more typical regions of the nebulae, far away from the complex regions near the centres of the galaxies. Although the surface brightness is lower, the expectation is that the physical processes at work are simpler and therefore easier to understand. The Horseshoe filament in NGC 1275, or more particularly the bright knot in that region known as Region 11 in the notation of Conselice, Gallagher, & Wyse (2001), is at a radial distance of 22 kpc (62 arcsec) from the centre of the galaxy and has an emission-line spectrum characteristic of large areas of the emission line nebulae (Hatch et al. 2006). There are several key diagnostics which set these regions apart from most other astrophysical emission line regions: First, the molecular hydrogen lines are very strong relative to the Balmer or Paschen lines of hydrogen, and certainly much stronger than can be produced in a photo-dissociation region such as the Orion bar (Hatch et al. 2005; Ferland et al. 2008). Second, the forbidden [NI] doublet at λ 5199Å is unusually strong, being typically $0.25 \times H\beta$ (Ferland et al. 2009). Third, the [NeIII] lines, both in the optical at

* E-mail: rmj@ast.cam.ac.uk

$\lambda 3869\text{\AA}$, and in the mid-infrared at $\lambda 15.55\mu\text{m}$ are stronger than expected while the $[\text{OIII}]\lambda\lambda 4959, 5007$ lines are typically very weak (Ferland et al. 2009).

2 PARTICLE HEATING

Ferland et al. (2009) used the code CLOUDY to calculate the *constant pressure* emission-line spectrum from Region 11 of the NGC 1275 nebula in which the excitation and ionization of the filaments was driven purely by collisions with ionizing particles. (The background level of starlight relevant to the galaxy environment of the nebula was included for completeness but had minimal effect due to its low intensity and an assumed self-shielding equivalent Hydrogen column density of 10^{21} cm^{-2} .) That model was able to reproduce the strengths of the commonly observed emission lines (including the key diagnostics mentioned above) within a factor of two, using only one free parameter, a power-law slope constraining the relative amounts of hot and cold gas.

In the physical model, the target cool gas exists at a range of densities and temperatures that are in pressure equilibrium with the surrounding X-ray emitting intracluster medium gas. Particle ionization can occur at a range of rates. To obtain the predicted spectrum, a grid of models was calculated covering a range of target gas densities and a range of ionizing particle fluxes. A weighted sum of these models was taken along a locus of constant pressure ($nT = 10^{6.5}\text{ cm}^{-3}\text{ K}$) matching that of the intracluster medium at Region 11. The weighting factors were constrained so that the cumulative volume filling factor at each temperature varied as a power-law in density of index α . α was the only free parameter in the model; it was set to reproduce the observed ratio of $\text{H}_2 12.28\mu\text{m} / \text{H}\alpha = 0.03$.

In Ferland et al. (2009) this model is referred to in some places as the ‘cosmic rays’ model to distinguish it from a separate model that was considered in which only thermal heat was injected in to the gas. In practice, all that is required in the particle heating model are particles with kinetic energies several times the ionization energy of Hydrogen; relativistic particles or actual cosmic rays are not required. Observations of NGC 1275 (Fabian et al. 2003) and NGC 4696 (Crawford et al. 2005) have shown a detailed spatial correspondence between the coolest observed X-ray emitting gas and $\text{H}\alpha$ emitting filaments leading Fabian et al. (2011) to discuss the possibility that the particles involved in exciting the emission lines may be those of the hot intracluster medium surrounding the filament.

3 FAR ULTRAVIOLET EMISSION DIAGNOSTICS

The far ultraviolet waveband is a crucial region for exploring the heating mechanism in these filaments. Recently, observations with the Hubble Space Telescope have revealed far ultraviolet emission that shows a good spatial correlation with emission-line nebulae (O’Dea et al. 2004; O’Dea et al. 2010; Sparks et al. 2009; Onk et al. 2011). Although this does indicate some star formation is present in some regions, this is probably not relevant to the bulk of the remote emission-line filaments; in particular, we note that although hot stars are very efficient at producing optical emission-line nebulae they are unable to reproduce the crucial emission-line diagnostics seen in central cluster galaxy filaments and referred to at the end of Section 1. Recently, Sparks et al. (2009) detected

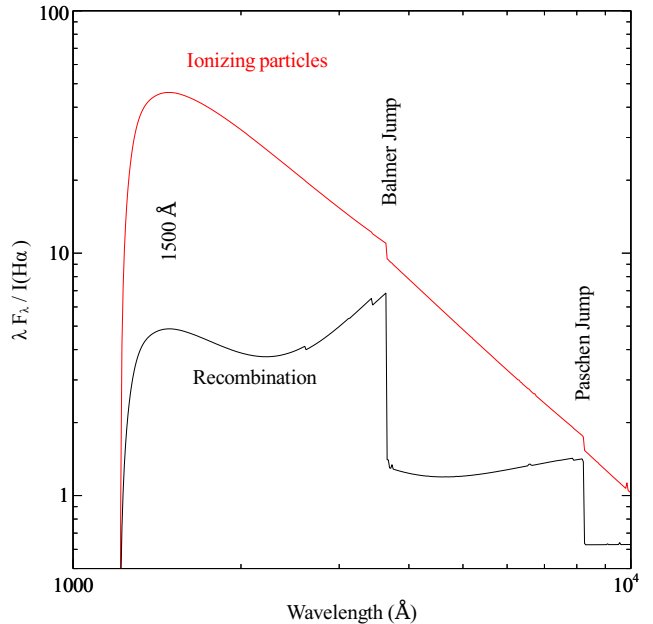


Figure 1. Comparison between emission produced by a photoionized gas (black line) and one energized by ionizing particles (red line). The continuous emission is given in terms of λF_λ (with units $\text{erg cm}^{-3}\text{ s}^{-1}$) divided by the intensity of $\text{H}\alpha$ in the same units. As a result the vertical axis is dimensionless, but could be changed to $F_\lambda / I(\text{H}\alpha)$ by dividing by the wavelength at each point. The ionizing particle case produces a far stronger two-photon continuum due to excitation to the $n = 2$ configuration by secondary non-thermal particles. In this case, the two-photon continuum dwarfs the broad recombination edges which are a hallmark of a photoionized gas and could easily mimic the continuum of a hot star.

far ultraviolet emission in the filamentary system around M87 using broad-band imaging. Follow-up spectroscopy by Sparks et al. (2012) has revealed this to be due to emission lines of $\text{CIV}\lambda 1550$ and $\text{HeII}\lambda 1640$. They interpret these lines as being formed in 10^5 K gas arising from thermal conduction between the hot 10^7 K and cold 10^4 K phases.

3.1 The continuum

A key prediction of our particle heating model is the continuum that is expected to be associated with the filaments. Since there is no incident photon continuum (apart from the weak metagalactic background flux) the only continuum emission associated with particle-heated filaments will be the diffuse continuum generated by atomic processes within the filament. The Hydrogen two-photon continuum is relevant to the far ultraviolet part of the spectrum.

Tests of our particle heating model show that the region with a temperature near $T \sim 10^4\text{ K}$ dominates the total H I two-photon emission due to the high emissivity at that temperature. Fig. 1 shows the 1000-10000 \AA spectrum from a single grid point in the particle heating flux / density plane with temperature $\sim 10^4\text{ K}$ in dimensionless units, λF_λ normalized by the $\text{H}\alpha$ flux from the same grid point.

The continuum spectrum produced by a low-density ($n_{\text{H}} = 100\text{ cm}^{-3}$) photoionized gas is also shown in the same panel for reference. The physics of line and continuum emission produced by photoionization followed by recombination is covered in Osterbrock & Ferland (2006). Case B conditions, where the Lyman lines

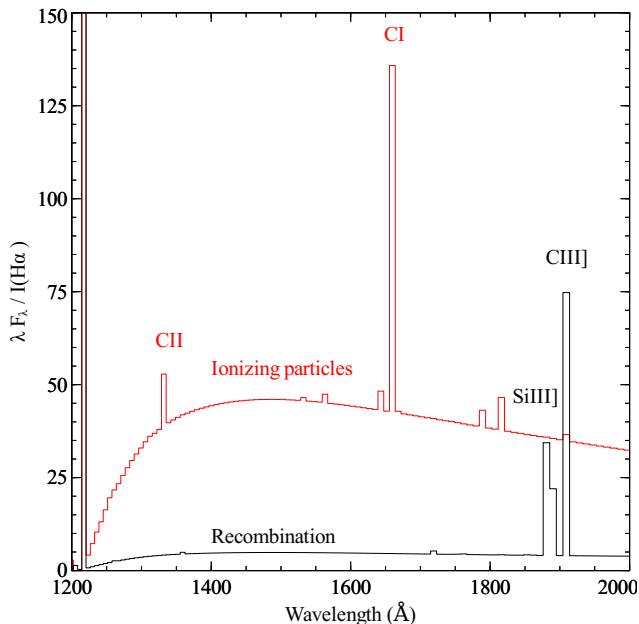


Figure 2. Far ultraviolet region of the spectra presented in Fig. 1. Note that the contrast of the emission lines against the continuum is dependent on the resolution of the spectrum and the intrinsic line width. Therefore the strength of the emission lines, whilst correct in a relative sense between emission lines in a spectrum is not to be simply read off from this spectrum.

are optically thick and higher series such as Balmer and Paschen are optically thin, should apply to the filaments. In Case B roughly one $H\alpha$ photon is produced for each H^+ recombination, and a third of recombinations eventually populate the $2s$ level that produces the two-photon continuum. The two-photon emissivity peaks, in terms of the photon flux at half the energy of $Ly\alpha$, or $\sim 2432 \text{ \AA}$, while in terms of energy flux the emissivity peaks at a slightly shorter wavelength near $\lambda 1500 \text{ \AA}$. Fig. 1 also shows two prominent recombination edges, the Balmer jump at $\sim 3646 \text{ \AA}$ and the Paschen jump at 8204 \AA , which are a hallmark of a photoionized gas.

A far stronger two-photon continuum is produced in the ionizing particle case relative to the emitted $H\alpha$ flux. Here the $H I$ emission is produced by non-thermal secondary electrons that excite atomic hydrogen from the ground configuration. The largest cross-sections are for excitation to the $n = 2$ configuration, which then produces $Ly\alpha$ and the two-photon continuum. The cross-sections for exciting to $n \geq 3$, which can decay and produce $H\alpha$, are much smaller. The result is that the two-photon continuum is roughly a factor of 10 stronger, relative to $H\alpha$, than is produced by photoionization followed by recombination. The emission is so strong in the ionizing particle case that the two-photon continuum dwarfs the recombination Balmer and Paschen edges. The blue / far ultraviolet spectrum is dominated by a strong continuum that might be mistaken for emission from a hot star if the cutoff at 1216 \AA was not covered in a spectrum.

3.2 The emission line of C I $\lambda 1656 \text{ \AA}$

In Fig. 2 we show the far ultraviolet part of the spectrum in more detail, on a linear scale appropriate for comparison with observations, and including line emission. (Note that the contrast of the emission lines against the continuum is dependent on the resolution of the spectrum and the intrinsic line width. Therefore the strength of the

emission lines, whilst correct in a relative sense between emission lines in a spectrum is not to be simply read off from this spectrum.) The particle heating model gives rise to a strong emission line from C I at $\lambda 1656 \text{ \AA}$ that is not seen in the recombination spectrum.

Dixon, Davidsen, & Ferguson (1996) presented a far ultraviolet HUT spectrum of NGC 1275 taken through a 9×116 arcsec slit passing through the galaxy nucleus at position angle 105° . C I $\lambda 1656 \text{ \AA}$ at the redshift of NGC 1275 ($z = 0.0176$) agrees well with the wavelength of the feature marked “Unk” in their figure 2 and listed as “Unidentified” in their table 2. The signal-to-noise ratio for this feature is low, and the slit is very large and passes through the bright nucleus. Nonetheless these data are suggestive of a detection of C I which could be confirmed in future HST observations.

The reason that the C I line is so strong in the particle heating model is due to the presence of suprathermal electrons in the regions where Carbon is neutral. Such suprathermal electrons are needed to collisionally excite this line which arises from an energy level 7.5 eV above the ground state and which would not normally be populated by a thermal distribution of particles where the temperature is low enough for Carbon to be neutral. This line and its formation mechanism is analogous to the [NI] doublet seen in the optical waveband at $\lambda 5199 \text{ \AA}$.

We note that the recombination spectrum shows lines of semi-forbidden Si III] $\lambda 1892$ and C III] $\lambda 1909$ which the particle heating model does not.

4 OBSERVATIONS AND DATA REDUCTION

In order to confront the particle heating model predictions for the ultraviolet continuum with observations we searched the Multimission Archive at the Space Telescope Science Institute (MAST) and Hubble Legacy Archives for ultraviolet spectra of Region 11 or images covering the region of the Horseshoe in NGC 1275. No ultraviolet spectra of this region are available, but there do exist ACS Solar Blind Channel images. We selected an image (data association id JA2703010) taken with the F140LP filter as most appropriate for this study due to its inclusion of the 1500 \AA peak of the Hydrogen two-photon continuum. Fig. 3 shows the relative system throughput for this configuration, with the spectrum predicted by the particle heating model presented in Fig. 2 overlaid.

Other supporting images used in this paper include our own ACS/WFC data (F625W) (to estimate the $H\alpha$ flux) already published in Fabian et al. (2008) and further WFPC2/F702W (to confirm the $H\alpha$ flux) and WFPC2/F814W (galaxy continuum) images downloaded from MAST. Details of the observations used are listed in Table 1.

The reduction of the F625W data have already been discussed in Fabian et al. (2008). The data downloaded from MAST is already fully reduced and we have used the final drizzled data products in this work. Data taken with HST at different epochs can have small offsets in the world coordinate systems due to the different guide stars used by the telescope. To align the zero points of the world coordinate systems of the data downloaded from the archive with our previously published images we applied a linear shift to register point sources with the ACS/F625W frame using the program GAIA from the Starlink Software Collection.

Fig. 4 shows a set of three images of an area of sky in the region of the Horseshoe filament. From top to bottom these images were taken through the F140LP, F625W and F814W filters. The two regions that we have analysed in this paper are indicated: the upper left circle (Region A) is centred on the bright knot of $H\alpha$

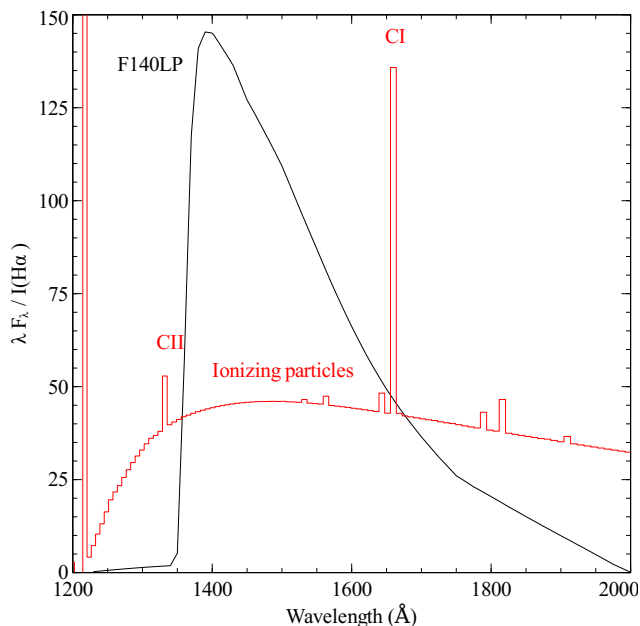


Figure 3. Relative system throughput for ACS/SBC with F140LP filter (solid black line), calculated from the STSDAS task BANDPAR. Overlaid in red, as a histogram plot, is the spectrum predicted by the particle heating model shown in Fig. 2.

emission at the base of the Horseshoe and corresponds closely to Region 11 in the work of Conselice, Gallagher, & Wyse (2001), while the lower right circle is Region B that we use to assess the background count rates.

5 ANALYSIS

Examination of the images presented in Fig. 4 reveals that the brightest part of the filamentary structure at the base of the Horseshoe seen in the F625W (emission line) image also shows up in the F140LP (ultraviolet) image.

In the following analysis we use a 1 arcsec radius circular aperture centred on the bright knot of emission located at RA(2000)=03:19:45.203, Dec(2000)=+41:31:33.41 as our best estimate of Region 11 of Conselice, Gallagher, & Wyse (2001).

5.1 Background subtraction

The filamentary structures seen in the nebula around NGC 1275 are superimposed on the underlying smooth emission from the galaxy stellar population. We note that in some spectral bands, in some spatial regions, emission and absorption from the infalling 8000 km s^{-1} system (Minkowski 1957; Burbidge & Burbidge 1965; Rubin et al. 1977) provides additional complexity. The Horseshoe region, however, appears to be clear of any contamination from the infalling system.

The F140LP data has not had any background subtracted from it, whereas the F625W data which is part of the mosaic published by Fabian et al. (2008) has had an approximate background, estimated from regions close to the edge of the component frames, subtracted.

In order to analyse the emission from Region 11 we need to remove not only the sky background, but also the underlying galaxy

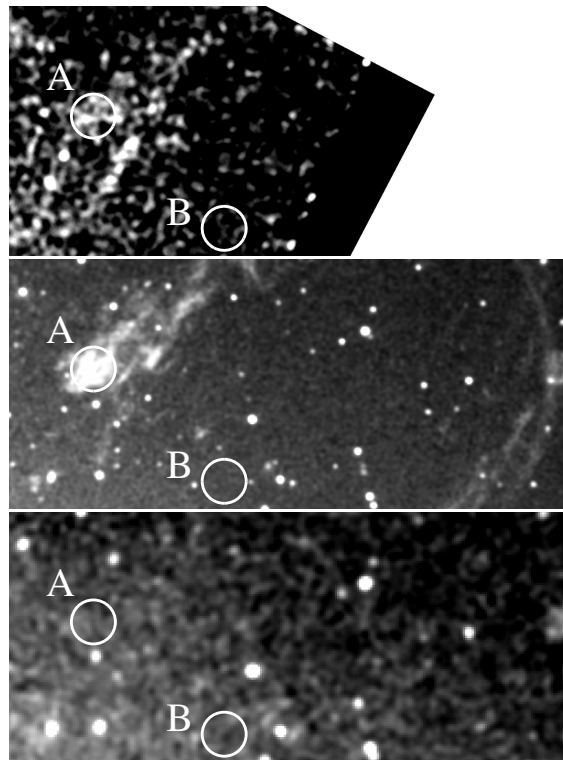


Figure 4. HST images of the north-west part of the NGC 1275 emission-line nebula, centred on the Horseshoe filament near RA(2000)=03:19:44.51 Dec(2000)=+41:31:32.5. Each frame is $25 \text{ arcsec} \times 11 \text{ arcsec}$; North is up, East to the left. From top to bottom the images are taken through filters F140LP, F625W and F814W. The images are displayed on a linear scale and have been smoothed with a gaussian kernel of sigma 0.275, 0.15, 0.3 arcsec respectively. The circles show regions A and B referred to in the text.

continuum. Under the assumption that the profile of the galaxy, and the flatness of the sky emission is the same in different filters, we can use an image free from emission lines to define a background Region B that has the same galaxy plus sky count rate as the region of interest, A. The F814W image fulfils this criterion well. The emission in the F814W filter which has a passband from approximately 7000 \AA to approximately 9600 \AA is expected to be dominated by light from the underlying elliptical galaxy due to the filter's very red bandpass and the fact that there are no strong emission lines at the redshift of NGC 1275 that occur within its bandpass. We confirmed that no filamentary structure is present in this filter under smoothing using a range of kernel sizes. A circular region, B, of radius 1 arcsec, located at RA=03:19:44.674, Dec=+41:31:28.31, within 10 arcsec of Region A, was found to have a count rate very similar to that of Region A (see Table 2) and is used as our background region in the other filters. We note that this method of background subtraction also removes any diffuse component of H α emission that might be present in the F625W image.

In Table 2 we show the count rates measured in regions A, B as well as the net count rate A-B in the four filters.

The F140LP data shows a background subtracted count rate of $0.12 \text{ e}^-/\text{s}$ in Region A, and yields approximately an 8σ detec-

Table 1. Log of Observations. * Due to the mosaicing of several pointing, not all of the image has the same exposure time. This is the exposure time for the Region A area.

Instrument	Data	Origin	Exposure Seconds
ACS/SBC/F140LP	ja2703010_drz_sci.fits	MAST/Hubble	2552
ACS/WFC/F625W	N/A	Fabian et al 2008	10751*
WFPC2/F702W	hst_06228_04_wfpc2_f702w_wf_drz.fits	MAST/Hubble Legacy	4700
WFPC2/F814W	hst_11207_a1_wfpc2_f814w_wf_drz.fits	MAST/Hubble Legacy	1600

Table 2. Measured Count Rates. * SBC data are in units of counts/s.

Instrument	Region A e ⁻ /s	Region B e ⁻ /s	Region A-B e ⁻ /s
ACS/SBC/F140LP*	0.3667	0.2427	0.12
ACS/WFC/F625W	47.463	10.438	37.03
WFPC2/F702W	18.52	8.19	10.33
WFPC2/F814W	57.47	57.24	0.23

tion. The F625W shows a net count rate of 37.0 e⁻/s. These counts come though a broad band filter, and, on their own are not simple to interpret.

5.2 Extinction corrections

NGC 1275 lies at a Galactic Latitude of -13° and is therefore relatively highly reddened by dust in our Galaxy. Many values of extinction have appeared in the literature. The NASA Extragalactic Database (NED) lists $E(B-V)=0.163$; Conselice, Gallagher, & Wyse (2001) use $E(B-V)=0.17$. We adopt this latter value in the current work and use the D Welch’s web form at <http://dogwood.physics.mcmaster.ca/Acurve.html> to calculate the absorption at specific wavelengths. This calculator, which is based on the formulae in Cardelli, Clayton, & Mathis (1989) requires, as input, the values of R_V , the ratio of total to selective absorption at V and A_V the total absorption in magnitudes at V. We adopt the commonly used value of $R_V=3.1$, and $A_V=0.527$, appropriate to $E(B-V)=0.17$.

5.3 Ultraviolet continuum flux

The ACS exposure time calculator (<http://etc.stsci.edu/etc/input/acs/imaging/>) with the two-photon continuum shape produced from CLOUDY, (see Section 6 and Fig. 8) redshifted and absorbed by a Galactic extinction of $E(B-V)=0.17$, indicates that for a uniform surface brightness source filling a 1 arcsec radius aperture, the observed count rate of 0.12 ct/s for Region A in the F140LP band is produced by a source with an intrinsic (extinction corrected) flux density of $1.28 \times 10^{-17} \text{ erg cm}^{-2} \text{ s}^{-1} \text{ \AA}^{-1}$ at 1500\AA .

We note that the morphology of the emission within Region A is close to a uniform surface brightness source, but not completely filling the aperture and with some bright knots. Running the exposure time calculator again, but assuming a point source morphology for Region A, yields a flux of $1.40 \times 10^{-17} \text{ erg cm}^{-2} \text{ s}^{-1} \text{ \AA}^{-1}$ for the same count rate, ie a flux that is 8 per cent brighter. Since the actual morphology is between the two extremes of a point source and a constant surface brightness source, but more like a constant surface brightness source than a point source we adopt the count rate

to flux conversion factor for a uniform surface brightness source and note that the emission line flux would be brighter, but by a lot less than 8 per cent if the actual morphology were used.

5.4 H α line flux

The ACS exposure time calculator (<http://etc.stsci.edu/etc/input/acs/imaging/>) indicates that for a single emission line at 6678.5\AA the redshifted wavelength of H α the observed count rate of 37.03 e⁻/s is produced with a line flux of $5.48 \times 10^{-15} \text{ erg cm}^{-2} \text{ s}^{-1}$. After correcting by a factor of 1.474 to account for Galactic reddening this gives an intrinsic flux of $8.1 \times 10^{-15} \text{ erg cm}^{-2} \text{ s}^{-1}$. If a point source had been assumed the observed flux would be $5.71 \times 10^{-15} \text{ erg cm}^{-2} \text{ s}^{-1}$, an increase of 4 per cent.

The F625W filter admits flux from the [OI], [NII] and [SII] doublets as well as the H α line (continuum emission in the filter band has been subtracted). In order to correct for these additional emission lines we use the relative strengths of these lines with respect to H α , published by Ferland et al. (2009). All the lines lie at wavelengths where the throughput of the F625W filter is near its maximum. The flux in the H α line is found to be 1/2.6 or 0.38 times the total line flux. The implied H α line flux is therefore $3.1 \times 10^{-15} \text{ erg cm}^{-2} \text{ s}^{-1}$.

5.4.1 Comparison with the emission line flux in Conselice, Gallagher, & Wyse (2001)

We note here that Region 11 in the work of Conselice, Gallagher, & Wyse (2001) is almost identical to our Region A. Their table 1 lists a flux for H α of $2.25 \times 10^{-14} \text{ erg cm}^{-2} \text{ s}^{-1}$. We assume that this flux includes the [NII] $\lambda\lambda 6548, 6584$ lines since they lie within the bandpass of their filter and there is no mention in the paper of correcting for the contribution from the [NII] lines. We further assume that the listed flux has been corrected for Galactic extinction following the prescription in their Section 2.

The passband listing for the KPNO filter KP1495 available at <ftp://ftp.noao.edu/kpno/filters/4inplots/kp1495.eps> used by Conselice, Gallagher, & Wyse (2001) shows that the redshifted H α line lies very close to the peak of the filter transmission. The [NII] $\lambda\lambda 6548, 6584$ lines also lie within 7 and 3 per cent of the maximum transmission respectively. We therefore assume that all the counts come from the wavelength of H α and note that the [NII] $\lambda 6548$ carries only one third of the flux in [NII] $\lambda 6584$ so the error in its calibration will be very minor.

Given the line ratios listed above, the extinction corrected H α flux in Conselice, Gallagher, & Wyse (2001) is inferred to be 1/1.95 times the total flux or $1.2 \times 10^{-14} \text{ erg cm}^{-2} \text{ s}^{-1}$. This is a factor of 3.9 larger than our extinction corrected flux.

In order to determine whether there is a flux calibration problem with our F625W data we identified four stars from the Hubble Guide Star Catalog (GSC) (version 2.3) which were faint enough to not be badly saturated, but bright enough to have magnitudes measured in several bands. Spectral energy distributions from a library of stellar models were convolved with the GSC bandpasses and fitted to the (j-N) colours of these stars for us by P Hewett. The best fitting spectral energy distribution, normalized to the F (red) magnitude was then input to the ACS imaging exposure time calculator (<http://etc.stsci.edu/etc/input/acs/imaging/>) to predict the count rate expected in the F625W data. Table 3 lists the stars together with their magnitudes and their predicted and observed count rates (both in circular apertures of radius 0.5 arcsec). In all cases the agreement is better than 33 per cent, (which is well within the uncertainties of the catalogue magnitudes) indicating that the factor of four discrepancy between our fluxes and those published by Conselice, Gallagher, & Wyse (2001) is likely not due to the F625W data. We note here that these measurements were made on intermediate product `single_sci` frames rather than the final mosaiced image since some of the stars are bright enough that the cosmic ray rejection algorithms applied to the final mosaic clip up to 15 per cent of the counts in the brighter stars. We spot checked the count rate in Region A in the mosaic and in the `single_sci` frames and found agreement within 5 per cent.

As an extra check on our calibration we have made a separate measurement of the emission-line flux from a WFPC2 data set taken with the F702W filter which covers the Horseshoe region. This filter also admits the [OI], [NII], and [SII] doublets as well as the H α line, so should yield a background subtracted flux very similar to the ACS F625W data. We note that these data were downloaded from the Hubble Legacy Archive and that the WFPC2 data products in this archive have been processed through the drizzling software using non-standard parameters, yielding images in units of electrons per second, rather than the default DN per second (http://hla.stsci.edu/hla_faq.html). We note also that the Fits header keyword BUNIT remains set to COUNTS/S despite the data being in units of electrons/s. Using the WFPC2 exposure time calculator at <http://www.stsci.edu/hst/wfpc2/software/wfpc2-etc-extended-source-v40.html> the net count rate of 10.33 cts/s for Region A in this instrument yields a line flux of 5.14×10^{-15} erg cm $^{-2}$ s $^{-1}$ in close agreement (~ 7 per cent) with the ACS F625W data for the same region (5.48×10^{-15} erg cm $^{-2}$ s $^{-1}$).

Privon et al. (2008) noted that extended emission-line regions in radio galaxies had lower fluxes when observed with HST WFPC2 compared with ground-based observations. They attributed this to a higher surface brightness detection limit due to the smaller pixels in the HST data. We note here that throughout this work we are measuring fluxes in the same size aperture as the fluxes presented by Conselice, Gallagher, & Wyse (2001) and therefore expect to obtain a consistent flux despite the lower surface brightness sensitivity of the HST data due to the smaller pixel size.

6 CONTINUUM EMISSION FROM THE PARTICLE HEATING MODEL

In this section we consider the interpretation of the continuum emission in terms of the particle heating model presented by Ferland et al. (2009). Hot young stars are unable to reproduce the op-

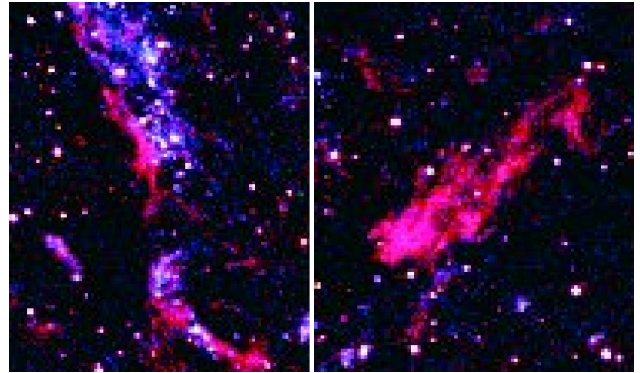


Figure 5. Comparison of two regions in the NGC 1275 nebula from observations published by Fabian et al. (2008). The red channel (F625W filter) includes emission from lines of [OI], H α , [NII] and [SII]; the blue channel (F435W filter) shows mostly blue continuum although it does include [OII] λ 3727 emission at a point in the filter transmission that has 40 per cent of the peak transmission. The left panel shows part of the South-West filament where there are nearby hot stars while the right panels shows the Horseshoe filament knot region with very few hot stars.

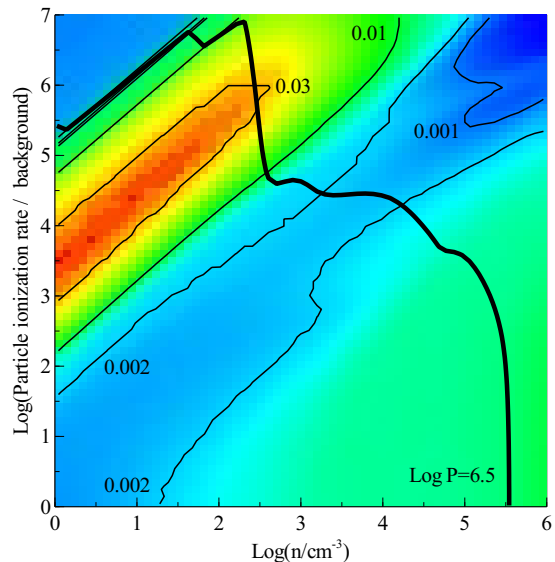


Figure 6. $R = F_{1500} / I(H\alpha)$ ratio for particle heating models explored by Ferland et al. (2009). Contour values are indicated. The locus of points with pressure $P=10^{6.5}$ cm $^{-3}$ K is shown by the thick black line.

tical emission-line ratios as discussed in Section 1. We also show here in Fig. 5 a comparison of two regions of the NGC 1275 nebula from the observations published by Fabian et al. (2008). These images are colour coded such that H α emission is red and blue continuum (F435W filter) is blue. Although there are some regions in the nebula where a luminous blue continuum is seen close to the H α emission (left panel, South-West filament) the Horseshoe filament knot (right panel) does not show such luminous blue emission, further suggesting that hot stars are not involved in exciting the emission-line gas.

In the particle heating models of Ferland et al. (2009), the relative amounts of gas at different temperatures was set using a

Table 3. Guide Star Catalogue Stars Data. Col 1: Catalogue star name; cols 2-5: magnitudes and uncertainties in the j, V, F and N bands; cols 6-7: predicted and observed count rates in circular aperture with radius 0.5 arcsec; col 8: percentage error between predicted and observed count rates.

Name	m_j	m_V	m_F	m_N	F625W(pred) e ⁻ /s	F625W(obs) e ⁻ /s	100×(pred-obs)/pred per cent
NCJ1022694	19.53±0.44	19.13±0.65	18.88±0.46	18.85±0.55	425.1	400.1	-6
NCJ1022527	19.83±0.45	19.27±0.77	19.10±0.47	19.11±0.61	334.6	222.9	-33
NCJ1022851	20.77±0.48	19.11±0.63	19.02±0.47	18.83±0.56	315.0	232.7	-26
NCJ1022049	19.71±0.45	19.19±0.73	18.95±0.46	18.89±0.56	389.4	324.9	-17

power-law to describe the cumulative filling factor of gas at a range of temperatures, their equation 14. The power-law slope ($\alpha=-0.35$) was set to match the ratio of the H_2 $12.28\mu\text{m} / H\alpha$ in Region 11 of the NGC 1275 nebula, but the $H\alpha$ flux used to set that ratio was derived from the Conselice, Gallagher, & Wyse (2001) data. The result from the previous section that suggests the fluxes from those data are too high by a factor of 3.9 has consequences for our predictions from this model. Reducing the $H\alpha$ flux by a factor of 3.9 requires a power-law slope $\alpha = +0.2$ to match the new value of H_2 $12.28\mu\text{m} / H\alpha=0.12$. A full treatment of the changes to the predictions from the particle heating model that this change of slope causes is beyond the scope of this paper and will be treated in a future paper.

For this paper, we have re-run the particle heating models explored by Ferland et al. (2009), using the development version of CLOUDY (newmole branch, revision 5792), in order to save the predictions for the continuum intensity as well as the $H\alpha$ flux, and use the new value of $\alpha = 0.2$.

The brightest part of the continuum is at $\sim 1500\text{\AA}$ so we have predicted the flux level expected in the Horseshoe knot at this wavelength. To set the normalization of the continuum emission we consider the ratio of weighted emissivities in the continuum at 1500\AA and the $H\alpha$ line.

In Fig. 6 we show how the ratio $R=F_{1500}/I(H\alpha)$ varies over the entire particle flux / Hydrogen density plane. Values ranging between 4×10^{-4} and 3.2×10^{-2} are produced in various parts of parameter space. It should be noted however that the emissivity and weighting factors vary considerably with temperature. The part of the diagram that we are interested in is the locus of models for which the gas pressure is $P=10^{6.5} \text{ cm}^{-3} \text{ K}$, shown by the thick black line. Fig. 7 shows how the ratio R, the emissivity of the $H\alpha$ line and the weighting function with the new value of $\alpha=0.2$, vary as a function of temperature along this constant pressure line.

To understand how the continuum to line ratio R varies across Fig. 7 we note that the $H\alpha$ intensity is proportional to the rate that the $n = 3$ configuration is populated while the two-photon continuum is proportional to the rate that the $2s$ level is populated multiplied by the fraction of these populations that decay to $1s$ rather than undergoing a collision to $2p$ (which then produces $L\alpha$).

The $2s$ term can be populated by collisions from $1s$ (mainly due to suprathermal electrons), recombination (either directly to $2s$ or indirectly by capture to higher levels followed by cascade to $2s$), and by collisions from $2p$. The relative importance of these processes depends on the relative abundances of suprathermal electrons, thermal electrons, and protons.

The variation in R is due to the remarkable changes in the physical conditions as we go across Fig. 7. The gas is almost fully molecular in the cold regions to the left, while it is moderately ionized in the warmest regions to the right. As an example, we consider three regions in Fig. 7, the two regions of peak $H\alpha$ intensity

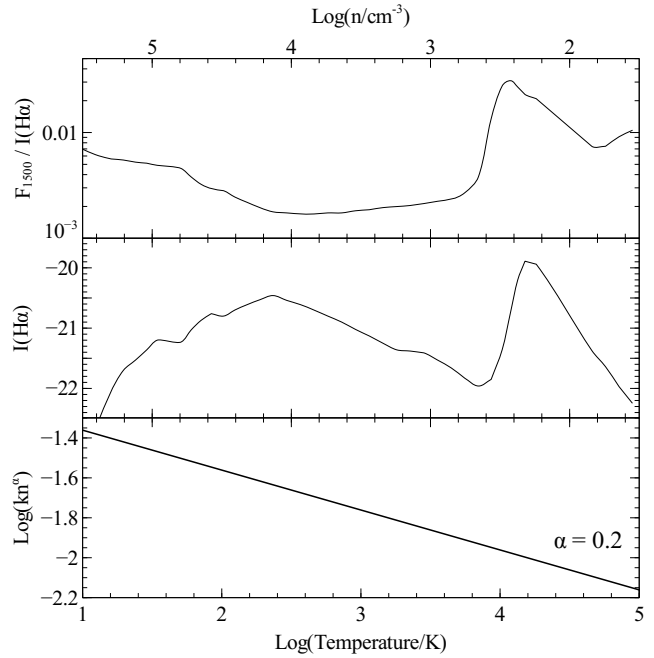


Figure 7. Values of $R = F_{1500} / I(H\alpha)$ (top panel), emissivity of $H\alpha$ (middle panel), and weighting function with $\alpha=0.2$ (lower panel) as a function of temperature for the particle heating models explored by Ferland et al. (2009), for the locus of grid points with pressure $P=10^{6.5} \text{ cm}^{-3} \text{ K}$.

and the lowest temperature point. At the highest temperature peak, near $\log T = 4.2$, Hydrogen has a density of $\sim 200 \text{ cm}^{-3}$ and is 22 per cent ionized with nearly all the rest atomic. At the $\log T = 2.4$ peak the Hydrogen density is much higher, 10^4 cm^{-3} but the gas is nearly entirely atomic. The ionized fraction is only 0.2 per cent. In the highest density case, $n \sim 3.2 \times 10^5 \text{ cm}^{-3}$ the gas is mostly molecular (91 per cent) with a tiny ionized fraction ($\sim 10^{-5}$ per cent). The curious result of this is that as the total Hydrogen density increases the electron density decreases, being $n_e = 48.4, 23.2,$ and 0.5 cm^{-3} at the three points. The resulting mix of physical processes causes the ratio R to vary in a non-monotonic manner.

To calculate the ratio R from the model we make a weighted sum of the $H\alpha$ and F_{1500} continuum emissivities along this constant pressure line between log temperatures of 0.5 to 4.5. The weighting factors are set by the power-law slope α . At some temperatures the gas is thermally unstable (Ferland et al. 2009) and must be excluded from the sum. These regions occur between values of log temperature between 1.5 and 1.9, and between 3.5 and 3.8. The final ratio, R is then determined by dividing the weighted emissivity in the continuum F_{1500} by the weighted emissivity of $H\alpha$. We obtain a value of 0.0082.

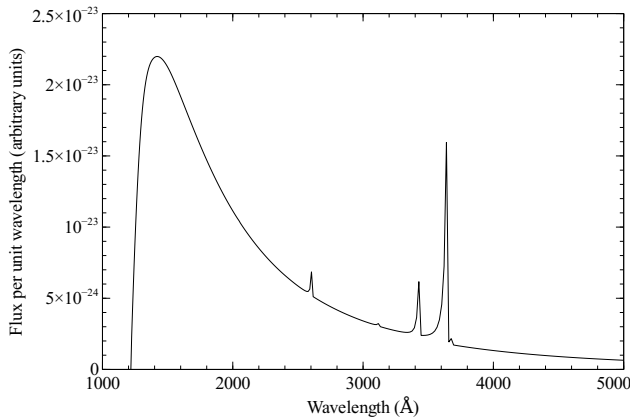


Figure 8. Spectrum of continuum emission produced by the particle heating model with $\alpha=0.2$, and pressure $P=10^{6.5} \text{ cm}^{-3} \text{ K}$.

Fig. 8 shows the predicted weighted spectral distribution of the continuum emissivity from the particle heating model over the wavelengths 1000-5000Å. There are several components to this spectrum. The brightest one is due to the Hydrogen two-photon continuum which peaks in the ultraviolet at $\sim 1500\text{Å}$ and has a sharp cutoff at 1216Å . Compared with Fig. 1 there are other contributions which come from the free-bound emission of Hydrogen, and Helium. The peaks at $\lambda\lambda 2600, 3433\text{Å}$ are due to HeI edges while the feature at $\lambda 3646\text{Å}$ is a blend of a HeI edge and the Hydrogen Balmer edge. We note that these peaks are much sharper than in the case of a recombination spectrum (Fig. 1) because they originate in much colder gas near the peak in $H\alpha$ emissivity at few $\times 100\text{K}$ (Fig. 7). Such sharp edges are a characteristic prediction of our particle heating model. They are not normally observed in the spectra of emission-line nebulae, but have been seen in the shell around nova DQ Her (Williams et al. 1978; Ferland et al. 1984). For further discussion of the continua see Section 3 of this paper and Osterbrock & Ferland (2006).

We note that from Section 3.1 the C I $\lambda 1656\text{Å}$ line is predicted to be the strongest emission line in the F140LP band. In our model the flux ratio of this line to $H\alpha$ is 0.2 so this line contributes less than 4 per cent of the counts in this band.

7 COMPARING THE RATIO $R=F_{1500}/I(H\alpha)$ BETWEEN MODEL AND OBSERVATIONS

If we ignore any intrinsic reddening within the filament we obtain the ratio of the far ultraviolet continuum at 1500Å to the $H\alpha$ flux, deduced from the HST imaging data, a value of $R = 4.1 \times 10^{-3} \text{Å}^{-1}$. This value is just half the value of $R=8.2 \times 10^{-3} \text{Å}^{-1}$ predicted by the particle heating model. We note here that although the observed fluxes have been corrected for reddening in our Galaxy, there is also reddening intrinsic to the filamentary system in NGC 1275. This can be seen by comparing the value of $I(H\beta)/I(H\alpha)=0.24$ (corrected for Galactic reddening) given in Table 5 of Ferland et al. (2009) with that predicted by the particle heating model, 0.271 (Table A1 of Ferland et al. 2009; this value is unchanged by the new value of α used in this work). Assuming a Galactic extinction law and using equations 1 and 2 of Canning et al. (2011), which make the simplifying assumption that the intrinsic reddening occurs in a screen in front of the Horseshoe filament, we determine an intrinsic $A_V=0.377$. This corresponds to extinction factors of 1.32 and 2.52

at the wavelengths of $H\alpha$ and 1500Å respectively. Applying this correction to the observed value of R increases it to $7.8 \times 10^{-3} \text{Å}^{-1}$, in very good agreement with that from the particle heating model.

We note here that were the Conselice, Gallagher, & Wyse (2001) value of the $H\alpha$ to be correct that the observed value of R corrected for both Galactic and internal reddening would be $R=0.002$, whereas the predicted value from the particle heating model with $\alpha = -0.35$ as published by Ferland et al. (2009) is a factor of nine higher at 0.018. The increase in R from the model comes from the higher weighting given to the high R region near $T=10^4\text{K}$ when $\alpha = -0.35$ while the decrease in observed R comes from the increase in $H\alpha$ flux.

8 CONCLUSION

We have shown that Region 11 in the Horseshoe filament of NGC 1275 is detected in the far ultraviolet at wavelengths of 1500Å by the Hubble Space Telescope ACS/SBC camera. The observed count rate is consistent with that expected from Hydrogen two-photon emission if the filaments are excited by ionizing particles. These particles could naturally originate from the cooler phases of the hot intracluster medium. In this region there is no requirement for any further components to the far ultraviolet emission from hot stars or emission lines such as CIV $\lambda 1550$ from intermediate temperature (10^5K) gas. Our particle heating model predicts a C I $\lambda 1656\text{Å}$ emission line at about $0.2 \times I(H\alpha)$ which is not expected in a nebula spectrum dominated by recombination processes.

9 ACKNOWLEDGMENTS

ACF acknowledges support by the Royal Society. RMJ and REAC acknowledge support from the Science and Technology facilities Council. GJF acknowledges support by NSF (0908877; 1108928; & 1109061), NASA (07-ATFP07-0124, 10-ATP10-0053, and 10-ADAP10-0073), JPL (RSA No 1430426), and STScI (HST-AR-12125.01 and HST-GO-12309). PvH acknowledges support from the Belgian Science Policy office through the ESA PRODEX program.

We thank Paul Hewett for producing spectral energy distributions from the magnitudes tabulated for the GSC stars.

Some of the data presented in this paper were obtained from the Multimission Archive at the Space Telescope Science Institute (MAST). STScI is operated by the Association of Universities for Research in Astronomy, Inc., under NASA contract NAS5-26555. Support for MAST for non-HST data is provided by the NASA Office of Space Science via grant NNX09AF08G and by other grants and contracts.

REFERENCES

- Burbidge E. M., Burbidge G. R., 1965, ApJ, 142, 1351
- Canning R. E. A., Fabian A. C., Johnstone R. M., Sanders J. S., Conselice C. J., Crawford C. S., Gallagher J. S., Zweibel E., 2010, MNRAS, 405, 115
- Canning R. E. A., Fabian A. C., Johnstone R. M., Sanders J. S., Crawford C. S., Ferland G. J., Hatch N. A., 2011, MNRAS, 417, 3080
- Cardelli J. A., Clayton G. C., Mathis J. S., 1989, ApJ, 345, 245

- Conselice C. J., Gallagher J. S., III, Wyse R. F. G., 2001, *AJ*, 122, 2281
- Crawford C. S., Hatch N. A., Fabian A. C., Sanders J. S., 2005, *MNRAS*, 363, 216
- Di Matteo T., Johnstone R. M., Allen S. W., Fabian A. C., 2001, *ApJ*, 550, L19
- Dixon W. V. D., Davidsen A. F., Ferguson H. C., 1996, *AJ*, 111, 130
- Fabian A. C., Sanders J. S., Crawford C. S., Conselice C. J., Gallagher J. S., Wyse R. F. G., 2003, *MNRAS*, 344, L48
- Fabian A. C., Johnstone R. M., Sanders J. S., Conselice C. J., Crawford C. S., Gallagher J. S., III, Zweibel E., 2008, *Nature*, 454, 968
- Fabian A. C., Sanders J. S., Williams R. J. R., Lazarian A., Ferland G. J., Johnstone R. M., 2011, *MNRAS*, 417, 172
- Farage C. L., McGregor P. J., Dopita M. A., 2012, *ApJ*, 747, 28
- Ferland G. J., Williams R. E., Lambert D. L., Slovak M., Gondhalekar P. M., Truran J. W., Shields G. A., 1984, *ApJ*, 281, 194
- Ferland G. J., Korista K. T., Verner D. A., Ferguson J. W., Kingdon J. B., Verner E. M., 1998, *PASP*, 110, 761
- Ferland G. J., Fabian A. C., Hatch N. A., Johnstone R. M., Porter R. L., van Hoof P. A. M., Williams R. J. R., 2008, *MNRAS*, 386, L72
- Ferland G. J., Fabian A. C., Hatch N. A., Johnstone R. M., Porter R. L., van Hoof P. A. M., Williams R. J. R., 2009, *MNRAS*, 392, 1475
- Hatch N. A., Crawford C. S., Fabian A. C., Johnstone R. M., 2005, *MNRAS*, 358, 765
- Hatch N. A., Crawford C. S., Johnstone R. M., Fabian A. C., 2006, *MNRAS*, 367, 433
- Hatch N. A., Crawford C. S., Fabian A. C., 2007, *MNRAS*, 380, 33
- Johnstone R. M., Fabian A. C., Nulsen P. E. J., 1987, *MNRAS*, 224, 75
- Johnstone R. M., Fabian A. C., 1988, *MNRAS*, 233, 581
- Johnstone R. M., Hatch N. A., Ferland G. J., Fabian A. C., Crawford C. S., Wilman R. J., 2007, *MNRAS*, 382, 1246
- Minkowski R., 1957, *IAUS*, 4, 107
- O’Dea C. P., Baum S. A., Mack J., Koekemoer A. M., Laor A., 2004, *ApJ*, 612, 1310
- O’Dea K. P., et al., 2010, *ApJ*, 719, 1619
- Oonk J. B. R., Hatch N. A., Jaffe W., Bremer M. N., van Weeren R. J., 2011, *MNRAS*, 414, 2309
- Osterbrock D. E., Ferland G. J., 2006. “Astrophysics of Gaseous Nebulae”, Second Edition, University Science Books, Sausalito, California.
- Privon G. C., O’Dea C. P., Baum S. A., Axon D. J., Kharb P., Buchanan C. L., Sparks W., Chiaberge M., 2008, *ApJS*, 175, 423
- Rubin V. C., Oort J. H., Ford W. K., Jr., Peterson C. J., 1977, *ApJ*, 211, 693
- Sparks W. B., Pringle J. E., Donahue M., Carswell R., Voit M., Cracraft M., Martin R. G., 2009, *ApJ*, 704, L20
- Sparks W. B., Pringle J. E., Carswell R. F., Donahue M., Martin R., Voit M., Cracraft M., Manset N., Hough J. H., 2012, *ApJ*, 750, L5
- Williams R. E., Woolf N. J., Hege E. K., Moore R. L., Kopriva D. A., 1978, *ApJ*, 224, 171

This paper has been typeset from a $\text{\TeX}/\text{\LaTeX}$ file prepared by the author.